Article

Duplex Stainless Steels for Thermal Energy Storage: Characterization of Oxide Scales Formed in Carbonate Salts at 500 °C

Miguel Morales [1,2,*] , **Sandra Gordon** [1,2], **Óscar Fernández-Arana** [1,2], **Fernando García-Marro** [1,2], **Antonio Mateo** [1,2] , **Luis Llanes** [1,2] **and Gemma Fargas** [1,2]

1   CIEFMA, Department of Materials Science and Engineering, EEBE, Universitat Politècnica de Catalunya, UPC, C/Eduard Maristany, 10-14, 08019 Barcelona, Spain
2   Barcelona Research Center in Multiscale Science and Engineering, Universitat Politècnica de Catalunya, UPC, C/Eduard Maristany, 10-14, 08019 Barcelona, Spain
*   Correspondence: miguel.morales-comas@upc.edu

Abstract: Next generation concentrated solar power (CSP) plants promise a higher operating temperature and better efficiency. However, new issues related to the corrosion against protection of the construction alloys need to be solved. In this work, two different duplex stainless steels grades, namely 2205 (DS2205) and 2507 (DS2507), were evaluated for their compatibility with the eutectic molten salt mixture of Li_2CO_3-K_2CO_3-Na_2CO_3 at 500 °C in air for thermal energy storage applications. Corrosion tests combined with complementary microscopy, microanalysis and mechanical techniques were employed to study the oxide scales formed on the surface of the duplex steels. The corrosion tests evidenced that the attack morphology in both duplex steels was a uniform oxidative process without localized corrosion. DS2507 presented a better corrosion resistance than DS2205, due to the formation of thinner, compact and continuous oxide layers with higher compositional content in Cr, Ni and Mo than DS2205. The oxide scales of DS2507 showed more remarkable mechanical integrity and adhesion to the metallic substrate.

Keywords: concentrated solar power (CSP); thermal energy storage (TES); molten salts; duplex stainless steel; oxide scales; high-temperature corrosion

1. Introduction

Concentrated solar thermal power (CSP) plants with a thermal energy storage (TES) system are considered a promising future technology for a renewable energy system, because of their high efficiency, low operation cost and great scale-up potential [1–3]. However, the intermittency of solar energy is a critical issue in this technology, and therefore, TES is a key component in CSP plants [1,4]. TES is typically composed of a storage medium, heat transfer equipment and a containment system [5,6], which holds the storage medium and energy transfer equipment [7]. Currently, commercial CSP plants typically employ molten nitrate salts (300–400 °C) as a thermal storage medium. To decrease the electricity cost of these plants, a next generation CSP technology, with a higher operation temperature range (550–700 °C) and a better energy efficiency, has been developed [8–13]. In this context, molten salts with higher melting temperatures are required to be employed in the storage system [14,15]. Chloride salts are very interesting due to their low cost [9,16,17]. However, their use presents several critical issues associated with their performance and long-term reliability such as the chloride salt formulation, and the potential corrosion problems of containment materials, since they are typically made of stainless steels [9].

Currently, the mixtures of carbonates are an interesting alternative to chloride salts due to their lower corrosive potential [14]. Several recent studies have evaluated molten carbonates as a promising heat transfer fluid for high temperature applications [18–20].

Carbonates such as nitrates possess a high heat capacity and great energy density, and therefore, require a smaller tank volume. However, carbonate salts present some technological issues such as a high melting temperature (around 400 °C), high cost and also certain corrosive potential. Compared to nitrate and chloride salts, carbonates are more expensive due to the high price of lithium carbonate [21], which depends on lithium demand for the battery market [22,23]. However, the lithium demand could decrease in the near future, due to the strong efforts carried out to replace lithium with other metal alternatives in battery technology [24,25]. Therefore, carbonate molten salts could be a viable alternative in the mid- and long-term. In this scenario, the eutectic mixtures of Li_2CO_3-K_2CO_3-Na_2CO_3 may be a promising high temperature heat transfer fluid and storage medium for molten salt in CSP plants above 650 °C [26,27].

Despite the potential of molten carbonate salts for the next generation of CSP technology, to the best of the authors' knowledge, only a few works in the open literature have reported the compatibility of CSP construction materials with ternary eutectic carbonate molten salts. Sarvghad et al. [28,29] studied three different steel grades and the Inconel 601 superalloy with the eutectic mixtures of Li_2CO_3-K_2CO_3-Na_2CO_3 at 450 °C in air for thermal energy storage. After 120 h, the attack morphology on the surface of all materials was uniform with no localized corrosion. Corrosion resistance decreased in the following order: Inconel 601 superalloy, austenitic stainless steel AISI 316 and duplex stainless steel 2205. M.T. de Miguel et al. [30] studied the compatibility between austenitic steel HR3C and eutectic ternary carbonate salt at 700 °C, which presented a multilayer formation composed of several Li-mixed oxides as corrosion products. Gallardo-González et al. [31] demonstrated that the initial corrosion rate of AISI 316 stainless steel at 600 °C was lower at higher amounts of lithium carbonate present in the molten salts mixture. More recently, Sah [32] presented the effect of the dissolution of corrosion products for the corrosion resistance of SS304 in molten Li_2CO_3-K_2CO_3-Na_2CO_3 eutectic at 650 °C. Moreover, recently Prieto et al. [27] reported the corrosion behavior of different construction materials in contact with the ternary eutectic Li_2CO_3-K_2CO_3-Na_2CO_3 salt: two austenitic stainless steel (AISI 310 H and AISI 347H), two nickel-base alloys (Haynes 214 and Haynes 230) and Kanthal, which is a Fe-Cr-Al alloy. Among the selected materials, stainless steel 347 showed the worst corrosion rates at 700 °C, and Kanthal exhibited the best stability. Alternatively, other works have recently proposed several strategies, such as adding Al [33] and spray-graphitization [34], to mitigate the corrosion of austenitic stainless steels immersed in molten Li_2CO_3-K_2CO_3-Na_2CO_3 salts.

Taking into consideration these previous works, additional corrosion studies should be carried out to find new alloys as CSP construction materials for thermal energy storage using ternary eutectic carbonate molten salts. In this sense, duplex stainless steels may be promising candidates to be used in those components of CSPs, such as tanks of carbonate salts, that require good corrosion resistance at working temperatures as high as 450 °C [28,35]. Since duplex steels consist of austenite and ferrite phases in close contents, they can achieve a better corrosion resistance than ferritic stainless steels, and a higher mechanical strength than the austenitic grades [36–38]. In addition, their corrosion behavior is closer to that of the AISI 316 [39]. In the annealed condition, the yield strength of austenitic AISI 316 reaches around 280 MPa, whereas duplex 2205 and superduplex 2507 present values higher than 450 MPa and 550 MPa, respectively [38]. On the other side, the effects of manufacturing, annealing and welding processes on the microstructure, mechanical properties and corrosion resistance of duplex stainless steel bulk and weldment components have been widely studied in the last decades [40–45], enabling the manufacturing of reliable construction components. For these reasons, duplex stainless steels are extensively used in many different applications such as building structures [46], superheater tubes in municipal solid waste incineration plants [47], industrial food [48], gas and petrochemical industry [49], among others.

In the present work, the corrosion behavior of duplex steel 2205 (DS2205) and superduplex steel 2507 (DS2507) were evaluated, for the first time, for their compatibility

with eutectic Li_2CO_3-K_2CO_3-Na_2CO_3 molten salt at 500 °C under an air atmosphere over the long-term. In doing so, oxide scales formed on the surface of the alloys exposed to the molten salts were characterized using complementary microscopy and microanalysis techniques such as X-ray diffraction, Raman spectroscopy and scanning electron microscopy (SEM). In addition, special attention was paid to the adhesion of the oxide layers to the metallic substrate, their mechanical integrity and surface roughness, since these properties could be crucial to mitigate the corrosion of these alloys in contact with molten salts.

2. Materials and Methods

The materials used in this study were a commercial EN 1.4462 DSS, equivalent to AISI S31803, provided by UGINE and ALZ (Arcelor Mittal Group, Luxembourg city, Luxembourg) for DS2205, and a commercial EN 1.4410 DSS, equivalent to UNS S32750 and commercial designation SAF 2507, provided by Sandvik AB for DS2507. The nominal compositions of the ferritic/austenitic stainless steels used for the corrosion tests are detailed in Table 1. The DS2205 specimens were supplied in the form of plates of $40 \times 20 \times 2$ mm^3. The DS2507 was supplied in the form of bars of 20 mm in diameter, which was machined to obtain cylindrical specimens 2 mm in width. The specimens were ground with SiC grinding paper, 1200 grit (in grains of SiC per square inch), in order to remove the previous metal oxide layers adhered to the surface. Afterwards, the samples were weighed and cleaned by using ethanol in an ultrasonic bath. An optimized mixture of Li_2CO_3-K_2CO_3-Na_2CO_3 (32/35/33 wt.%) with a melting point of 397 °C was prepared using lithium carbonate 99% (CAS No. 554-13-2), potassium carbonate anhydrous LR (CAS No. 584-08-7) and sodium carbonate anhydrous LR (CAS No. 497-19-8) [50,51]. Previously, each carbonate salt was dried in a furnace at 180 °C for 48 h using an alumina crucible.

Table 1. Chemical composition (wt.%) of duplex stainless steels 2205 and 2507.

Alloy	Fe	Cr	Ni	Mo	Mn	C	N	Si	P	S
2205	Bal.	22.6	5.2	3.0	1.5	0.02	0.16	<0.45	<0.03	<0.015
2507	Bal.	25.0	7.4	3.8	<2.0	0.01	0.24	<0.8	<0.03	<0.015

Corrosion tests were performed by immersing the samples into the molten salt in alumina crucibles open to an air atmosphere at 500 °C in a preheated furnace. Test temperature was selected to be higher than the melting point of salt (397 °C) based on the assumption that the salt will be used as a PCM of a CSP plant for components working around 500 °C. Corrosion behavior was evaluated from oxide scale thickness at several exposure times (120, 300, 600, 1000 and 1600 h) for each alloy measuring the oxide layer and metal thicknesses with an optical microscope (Olympus, Tokyo, Japan) and a field emission scanning electron microscope (FESEM, Carl Zeiss Merlin, Oberkochen, Germany). Additionally, the evolution of oxide scale growth was complementarily determined through Eddy current loss using a defectometer (Defectometer M 1.837, Foerster, Tokyo, Japan) to determine the oxide layer thickness in different regions of at least 3 samples. The response of Eddy current loss associated with the oxide scale thickness for each alloy was calibrated by using different oxide layers with thicknesses measured by SEM.

In order to determine the protective character of oxide layers formed on the duplex steels, a compositional and microstructural analysis of the cross-sectional oxide scales was carried out using a FESEM equipped with Energy Dispersive Spectroscopy (EDS) (Oxford Instruments INCA-350 system, Abingdon, UK). For this purpose, the cross-section of samples was ground and then polished with diamond suspensions of decreasing particle size (30–6–3 µm). The crystalline phases at the surface of samples were determined with X-ray Diffraction (XRD, Bruker, D8-Advance, Billerica, MA, USA) using Cu Kα radiation (operated at 40 kV and 40 mA) and Raman Spectroscopy (inVia Qontor, Renishaw, Wotton-under-Edge, UK). For Raman spectroscopy, two lasers with different wavelengths of the applied excitation line were used: the first laser in the infrared region (785 nm) and

the second in the visible region (532 nm). An optical microscope with 100× objective was employed to determine the analysis zone. On the other side, scratch tests were performed using a scratch tester (CSM Instruments Revetest, Needham, MA, USA) with a Rockwell C diamond indenter of 200 μm radius. Tests were performed under progressive loading from 0.9 N up to 80 N in a 5 mm scratch length with 6.32 mm/min loading speed rate. Finally, the surface topographic profile of the oxide scales was determined in 3 different regions of each sample, using a contact profiler (Dektak 150 Stylus, Bruker, Billerica, MA, USA). A tip with a radius of 50 nm was employed at a force of 15 mg for scanning a total length of 300 μm.

3. Results and Discussion

3.1. Evolution of Oxide Scale Growth

The evolution of the thickness of the oxide scales for duplex steels in molten carbonate salt at 500 °C was investigated to determine their corrosion resistance and clarify the effects of the composition of each alloy on corrosion behavior. Figure 1 shows the oxide layer thickness for DS2205 and DS2507, determined using optical microscopy and SEM, and also the Eddy current loss, as a function of the exposure time to molten salts. The oxide thickness of DS2205 presented a significant linear growth regime for the first 600 h, and then the corrosion curve described a diffusion limited regime. In contrast, the corrosion behavior of DS2507 exhibited a diffusion limited regime since the exposure time was as low as 120 h. Thus, the DS2507 presented a lower corrosion rate due to its higher elemental composition on Cr, Ni and Mo, as compared to DS2205. The oxide thickness measured by both methods was quite similar, demonstrating that the Eddy current loss depended on the oxide layer thickness. However, it was also sensitive to variations in the elemental composition of each steel, crystalline phases and defects, such as roughness, porosity and voids, formed at the oxide scales, among others. In addition, this non-destructive technique confirmed that the growth of the oxide layer was relatively uniform on all surfaces of the samples, as the oxide thickness values obtained at the edges and the central zones of samples were quite close in both steels. Thus, the Eddy current loss is a useful non-destructive method for determining the thickness, tendency and uniformity of corrosion in duplex stainless steels.
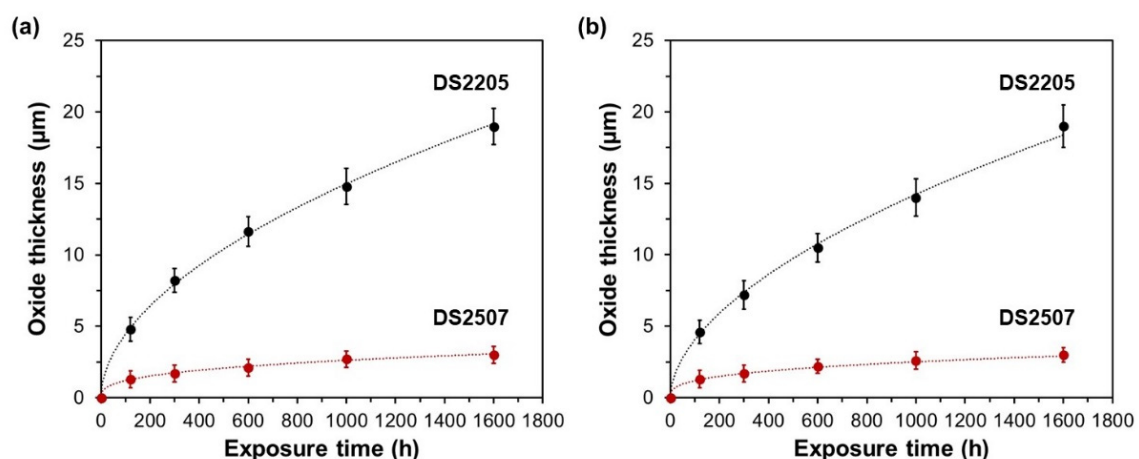

Figure 1. Evolution of oxide scale thickness formed on DS2205 and DS2507, as a function of the exposure time determined using: (**a**) optical microscopy, and (**b**) Eddy current loss method.

On the other hand, the growth of the oxide thickness as a function of exposure time evidenced a tendency of power law in both alloys (Figure 1a,b), which is a typical corrosion behavior with a diffusion limited regime. Therefore, it can be fitted to a time-dependent power law [52], as follows:

$$T = kt^n \tag{1}$$

where T is the oxide thickness (μm), t is the exposure time (h), and k and n are the fitting parameters indicating the rate constant and the exponent that determines the law of oxide growth kinetics, respectively. Thus, when n is close to 1.00, 0.50 and 0.33, the corresponding laws are linear, parabolic and cubic, respectively [53]. The obtained k and R-squared values of trend (R^2) for plots determined from Equation (1) are summarized in Table 2. The R-squared values were calculated to determine the reliability of the trend. The fitting results indicated that the relationships between oxide thickness and exposure time for duplex-exposed samples approximately followed parabolic ($n \approx 0.50$) and cubic ($n \approx 0.33$) growth kinetics, respectively. Taking into account the references of previous works [1,4,9,27], the DS2205 behavior suggested a good corrosion resistance immersed in molten carbonate salts at 500 °C. Meanwhile, the DS2507 obtained a corrosion rate ten times lower than DS2205, achieving a remarkable behavior against corrosion.

Table 2. Experimental parameters of Equation (1) after fitting the oxide thickness as a function of exposure time with each method for measuring of oxide thickness in the alloys. (*) Units of k expressed in μm·h$^{-1/2}$ for DS2205 and μm·h$^{-1/3}$ for DS2507.

Parameters	Optical Microscopy		Eddy Current Loss	
	DS2205	**DS2507**	**DS2205**	**DS2507**
k (*)	0.328	0.280	0.397	0.257
n	0.54	0.33	0.53	0.34
R^2	0.997	0.998	0.991	0.993

3.2. Crystalline Phases of Oxide Scales

Figure 2 shows the XRD spectra of DS2205 and DS2507 oxide scales, after 300 h and 1600 h of exposure to molten salts. The DS2205 spectrum for 300 h (Figure 2a) exhibited the substrate characteristic patterns of the duplex steel phases (α, γ and σ), and the peaks of oxide scale corresponding to chromium oxides (e.g., $FeCr_2O_4$, and $LiCrO_2$), iron oxides (e.g., $LiFeO_2$ and $LiFe_5O_8$), and NiO. Exposing the DS2205 for 1600 h, no significant change in the nature of oxide phases was observed, but their presence increased with the exposure time, since their relative peak intensities were augmented concerning duplex steel exposed for 300 h. On the other side, the DS2507 spectra after 300 h and 1600 h (Figure 2b) presented the typical α and γ superduplex phases that came from the metallic substrate, and the presence of the NiO phase was detected. In this case, the NiO patterns showed an increase in intensity with the exposure time, in a similar tendency of chromium and iron oxides phases in DS2205. However, other species such as $FeCr_2O_4$ and $LiFe_5O_8$ (detected in DS2205) were not clearly discerned in the superduplex samples, probably due to their absence and/or the smaller thickness of its oxide scales. Li-containing corrosion products, such as $LiFeO_2$, $LiFe_5O_8$ and $LiCrO_2$, were detected in the oxide scales of the steels, which is in a good agreement with previous works reported for other austenitic stainless steels under similar atmospheres [30,31,54–57]. The presence of $LiFeO_2$, and especially $LiFe_5O_8$, did not offer good protection against corrosion, due to the fact that this compound tends to form porous oxide layers, which can accelerate the corrosion process. In contrast, the formation of NiO and $FeCr_2O_4$ are considered to have a good protective character [57]. In both DS2205 and DS2507 alloys, the peak intensities of α phase decreased with the exposure time in a major proportion than γ phase. This may be attributed to the higher corrosion resistance of the γ phase compared to α, since the γ phase contains a higher Ni amount. The oxidation proceeds faster along the α phase, while the γ phase acts as a barrier against further oxidation forming a compact oxide layer that protects the underlying ferrite layer [28].
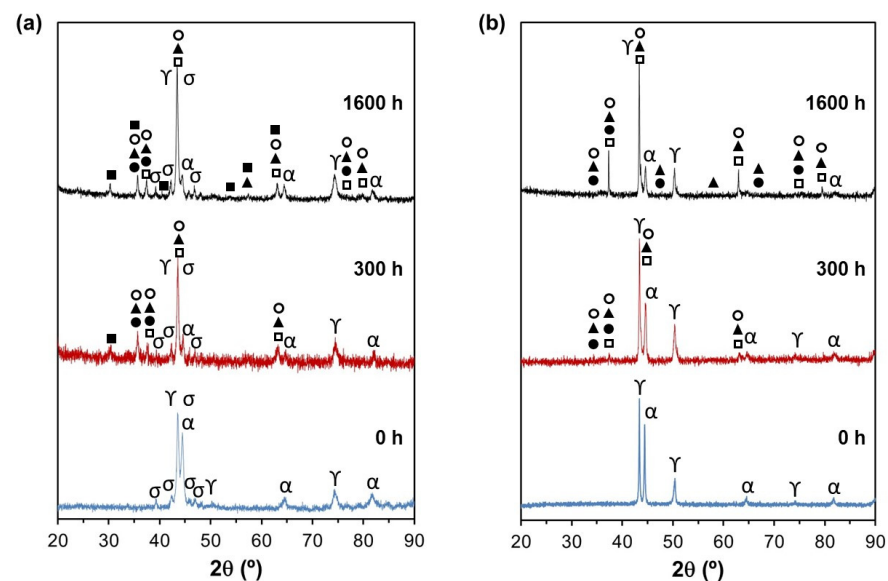
Figure 2. XRD spectra and peak identification chart of oxide scales formed on the surfaces of: (**a**) DS2205 and (**b**) DS2507, after several exposure times to molten salts. The symbols denote the phases: α, δ, γ and σ (of metallic substrate); chromium oxides (e.g., ● $FeCr_2O_4$, and ▲ $LiCrO_2$); iron oxides (e.g., ○ $LiFeO_2$ and ■ $LiFe_5O_8$); and □ NiO.

On the other hand, Figure 3 exhibited the Raman spectra of oxide scales, formed on DS2205 and DS2507, after several exposure times to molten salts. As shown in Figure 3a, the Raman spectra of both steels, in the infrared laser region, presented an intense and wide band at around 1350 cm^{-1}, which is characteristic of $LiFeO_2$, $FeCr_2O_4$, $LiCrO_2$ and NiO. In addition to these intense bands, a large number of bands with lower intensity for DS2205 samples were also observed in the range between 100 and 800 cm^{-1} for DS2205 samples. In order to analyze with more accuracy this spectral region, Figure 3b exhibited the Raman spectra of DS2205 in the visible laser region, which mainly confirmed the presence of $LiFeO_2$, $LiFe_5O_8$, $FeCr_2O_4$ and $LiCrO_2$. In a similar way to the XRD results, the Raman spectra of DS2507 samples did not show intense and well-defined bands in the range between 100 cm^{-1} and 900 cm^{-1}, probably due to the small thickness of DS2507 oxide scales. As expected, the results of XRD and Raman spectroscopy show the presence of numerous different phases in both oxide scales, due to the large number of alloying elements in the duplex steels.
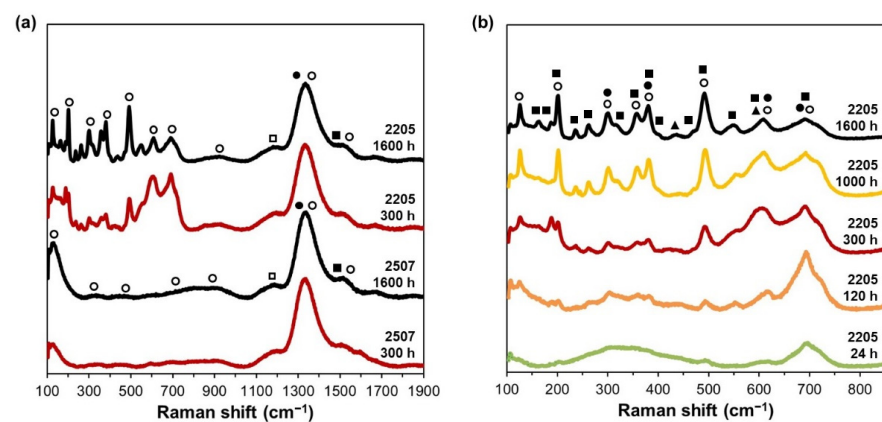

Figure 3. Raman spectra at: (**a**) infrared and (**b**) visible laser region, corresponding to oxide scales of DS2205 and DS2507 after several exposure times to molten salts. The symbols denote the phases: chromium oxides (e.g., ● $FeCr_2O_4$, and ▲ $LiCrO_2$); iron oxides (e.g., ○ $LiFeO_2$ and ■ $LiFe_5O_8$); and □ NiO.

3.3. Composition and Microstructure of Oxide Scales

Figure 4 shows the cross-sectional SEM images of DS2205 oxide scales formed for 300 h and 1600 h, which had a thickness of ~7 and ~18 μm, respectively. Both oxide scales presented some defects such as submicrometric pores, voids and vertical grooves. The formation of porosity may be attributed to the remarkable formation of $LiFeO_2$ and $LiFe_5O_8$ [54–57]. Figure 5 shows the SEM-EDS line scans of the oxide layers formed on DS2205 surface for 300 h and 1600 h. The scale formed for the shortest time presented a compositionally homogeneous layer, mainly formed by Fe with small amounts in other alloying elements (Figure 5a,b). In contrast, a double layer was observed on the surface of the sample exposed for the longest time (Figure 5c,d). While the outer layer was primarily composed of Fe and Cr oxides, the inner layer contained the oxides of Fe and Cr and, to a lesser extent, of Ni, Mo and Mn.
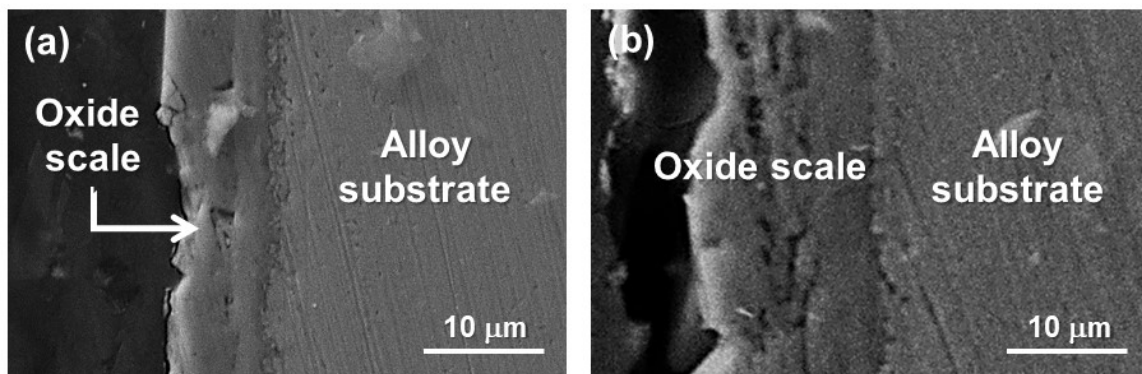

Figure 4. Cross-sectional SEM images of DS2205 samples exposed to molten salts for: (**a**) 300 h, and (**b**) 1600 h.
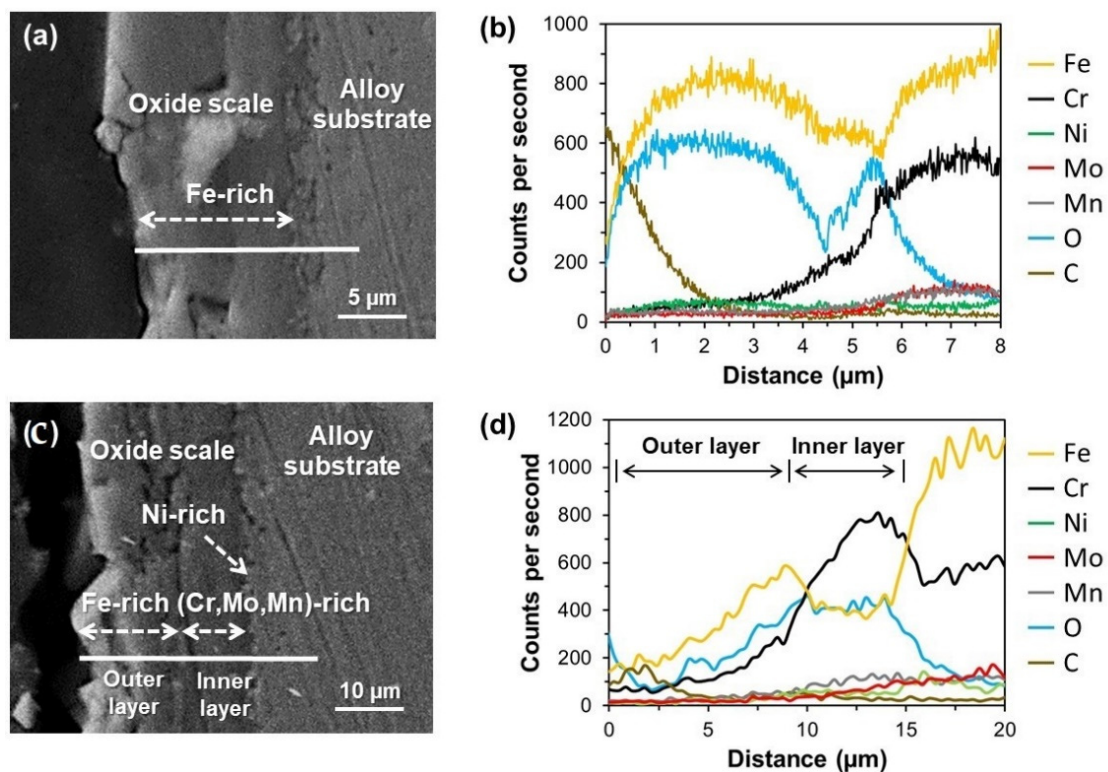

Figure 5. Cross-sectional SEM images and EDS line-scan analyses corresponding to the white line of DS2205 exposed to molten salts for: (**a,b**) 300 h, and (**c,d**) 1600 h.

On the other hand, Figure 6 shows the cross-sectional SEM images of DS2507 oxide scales generated for 300 h and 1600 h. A dense and continuous protective layer without remarkable defects was observed in the sample of 300 h (Figure 6a). After 1600 h, the oxide scale still presented a continuous and compact layer, but also exhibited few sub-micrometer pores and voids near the surface (Figure 6b). Compared to the DS2205 oxide layer, this compact scale with a good attachment to the DS2507 substrate led to an enhancement of the corrosion resistance in contact with the molten salts. Figure 7 shows the SEM-EDS line scans of the DS2507 oxide layers formed for 300 h and 1600 h. In this case, both oxide scales were composed of a double layer with an average thickness of ~1.5 μm for 300 h and ~3 μm for 1600 h. The inner layer presented a thickness of ~1 μm (for 1600 h), and was strongly enriched in Cr, Ni and Mo. The Fe-rich outer layer exhibited around 2 μm thickness (for 1600 h), which could explain the formation of some sub-micrometer pores and voids.

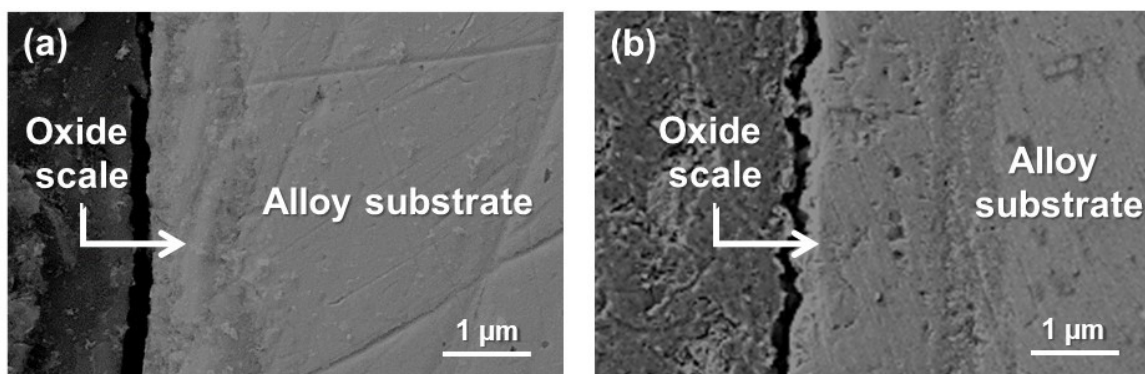**Figure 6.** Cross-sectional SEM images of DS2507 exposed to molten salts for: (**a**) 300 h, and (**b**) 1600 h.
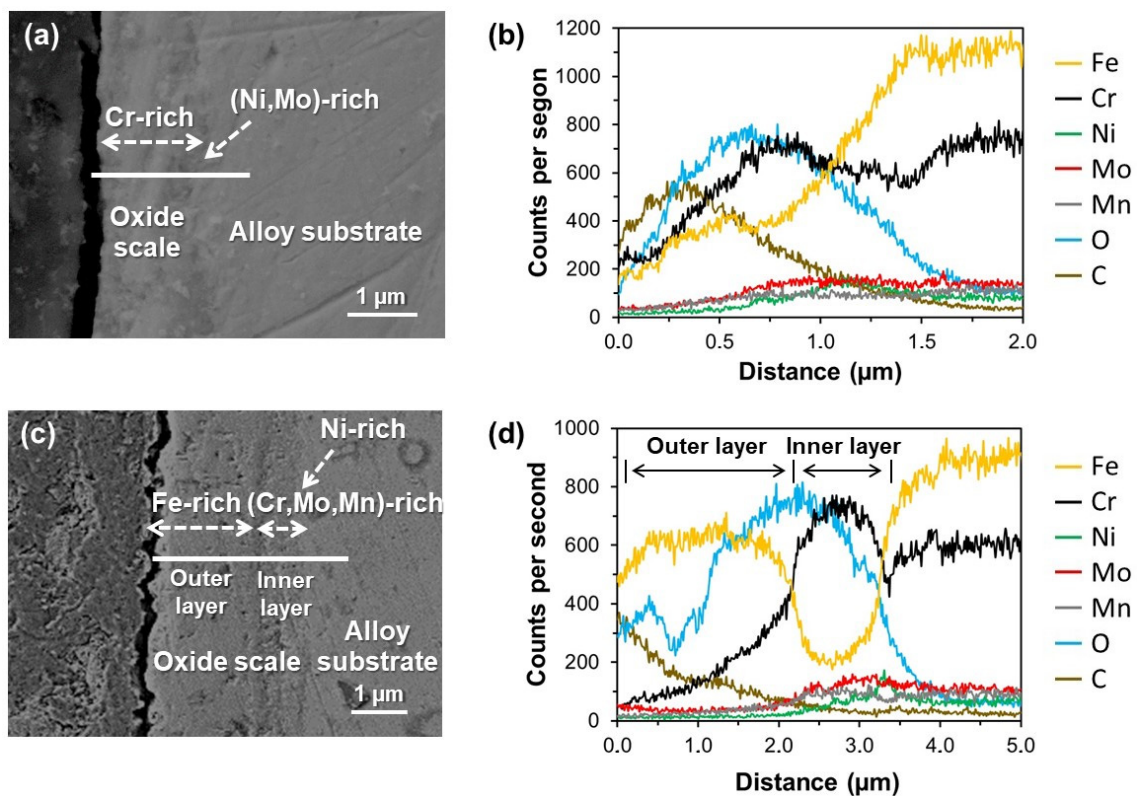

Figure 7. Cross-sectional SEM images and EDS line-scan analyses corresponding to the white line of DS2205 exposed to molten salts for: (**a**) and (**b**) 300 h, and (**c**) and (**d**) 1600 h.

In the growth process of oxide scales, the enrichment in Cr, Ni and Mo oxides near the oxide/metal interface of superduplex 2507, compared to duplex 2205, suggests that it could play an important role as a barrier against further oxidation, and also enhance the adhesion between the oxide scale and metallic substrate. Previous corrosion studies of DS2205 [28,39], which were carried out under atmospheres other than carbonate molten salts, reported that the presence of Mo at the oxide/metal interface influences the oxide growth in two ways: reducing the activity of Fe at the phase boundary, and also inducing a diffusion barrier for Fe and Cr ions between the oxide and the metal. In both duplex steels here studied, the absence of intergranular attack on the alloy surface, the non-depletion of the alloying elements, particularly in Cr and Ni, from grain boundaries, as well as the homogeneous morphologies of oxide scales demonstrated that the corrosion proceeded as a uniform oxidative attack on the alloy surface at long-term. However, the generation of the final double oxide layer could be formed in several stages (Figure 8). According to previous works [28,39], taking into account the composition of austenite (with higher Ni and Mo contents) and ferrite (with higher Cr content) in duplex stainless steels, at the initial oxidation stage (for the tens of hours), oxidation proceeds faster along ferrite while austenite acts as a barrier against further oxidation and protects the underlying ferrite layer. The presence of austenite as a nobler phase in the vicinity of ferrite may contribute to faster oxidation due to the galvanic corrosion of ferrite, acting the ferrite and austenite as anodic and cathodic electrodes, respectively. With the increase in oxidation time (until a few hundred hours), the amount of this compound increased until it was homogeneously distributed on the whole surface of the alloy, and therefore, the corrosion proceeded as a uniform oxidative attack. During the oxidation process in long-term, from 300 h to 1600 h, Cr was strongly accumulated at the inner layer, but also diffused from the inner oxide layer to the outer layer, and finally the content in Cr rich oxide was gradually distributed at the outer oxide layer. The distribution and extension of this compound at the oxide layer probably depended on the formation rate of diffusion barrier composed of Cr, Ni and Mo oxides at the oxide–metal interface. In addition, the presence of Li-containing corrosion products, such as $LiFeO_2$, and especially $LiFe_5O_8$, contributed to the formation of porous oxide layers, which can accelerate the corrosion process. Therefore, the oxide growth depends on the composition of each duplex stainless steel, justifying the differences of protection behavior observed in the oxide scales for each alloy.
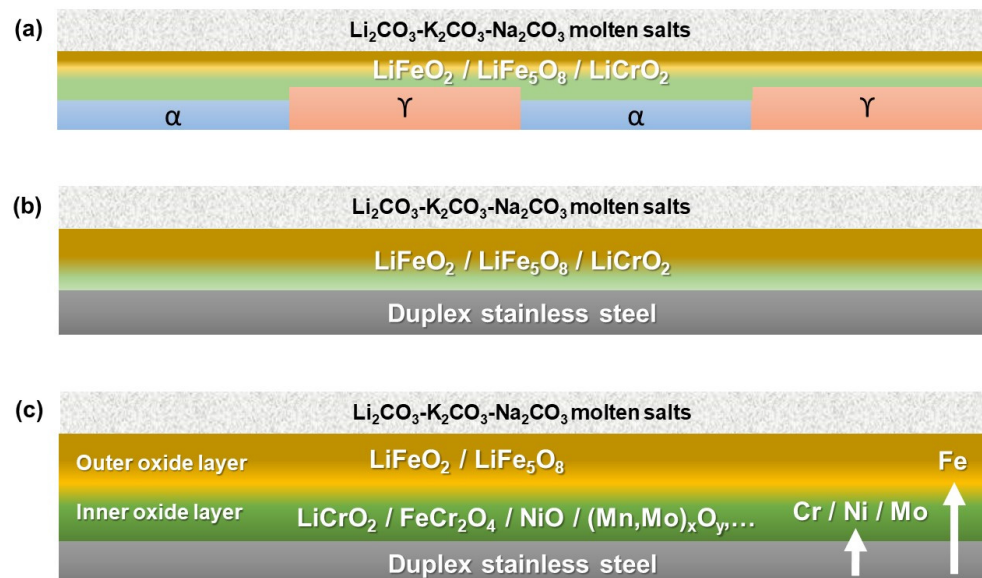

Figure 8. Scheme of the growth process of oxide scales in DS2205 and 2705 at: (**a**) the initial oxidation stage (after tens of hours) [28,29], (**b**) the increase in the oxidation time (until 300 h), and (**c**) the oxidation process at long-term (from 300 h to 1600 h).

3.4. Adhesion of Oxide Scales to Metallic Substrate

Generally, the corrosion resistance, and also particularly in molten salts, is also associated with a good mechanical integrity of the oxide scales as well as their adhesion to the metallic substrate, which avoids their detachment in operation and contributes to decreasing the corrosion process [58]. Thus, the analysis of the tracks of scratch test is a suitable way to determine their mechanical integrity and adhesion. Figure 9 shows the intermediate region of the scratch tracks for the oxide scales of both duplex alloys. Additionally, the scratch track of AISI 1020 carbon steel has been included for comparison purposes. This intermediate region of the scratch track containing three specific zones was deeply analyzed to study the failure mechanisms of oxide scale: (1) at the initial zone, containing mainly the oxide layer, allows a study of its mechanical integrity, (2) at the intermediate zone, where both the oxide layer and substrate coexist at the scratch valley, in order to determine the oxide–substrate adhesion, and (3) at the final zone, in which the substrate is only present at the scratch valley, to analyze the accumulation of oxide at both sides of the scratch, generating a remarkable pile-up with the oxide displaced during the scratch.
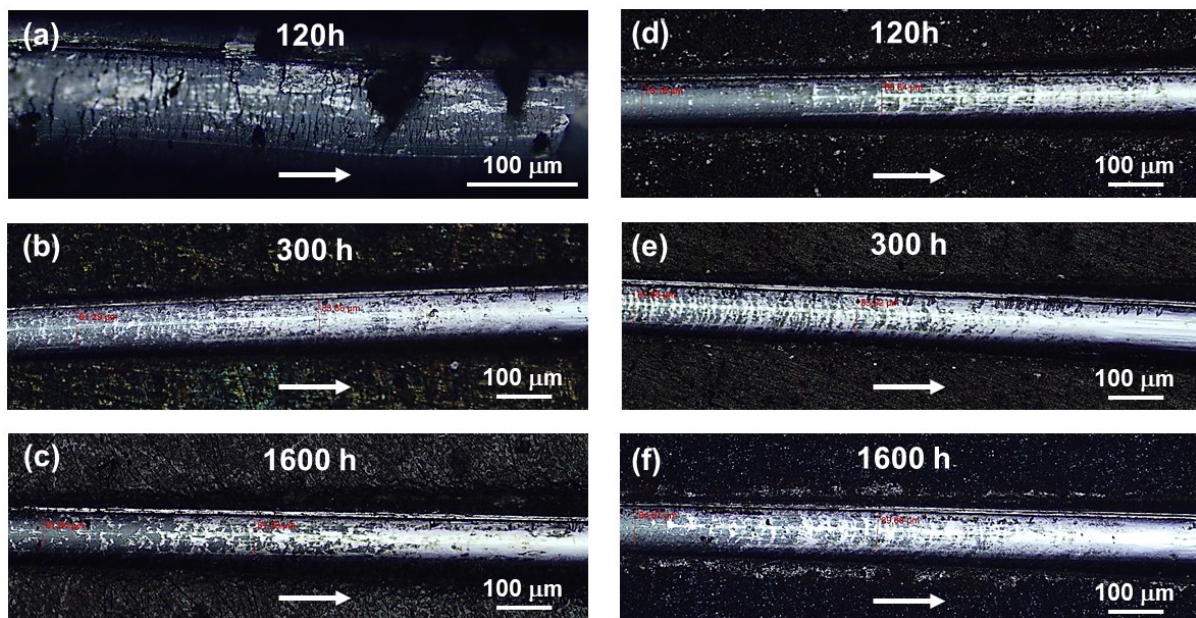

Figure 9. Optical microscopy images at the same intermediate region of scratch tracks on the oxide scale surface of: (**a**) AISI1020, (**b**,**c**) DS2507, and (**d**–**f**) DS2205, after several exposure times indicated in each image. The white arrow indicates the indenter sliding direction during the scratch test.

As shown in Figure 9a, the scratch track of AISI1020 on the oxide scale formed after 120 h, used as a reference, presented large transversal cracks at the oxide layer, and several zones with area spallation or gross spallation. These failure modes were typically attributed to poor oxide/metal adhesion as well as when the residual stress level in the scale was high, presenting a low mechanical integrity. In contrast, the progressive removal of oxide layer and without interface decohesion was observed in the scratch of both DS2507 samples (300 h and 1600 h) (Figure 9b,c). This failure mechanism, and the absence of defects and spallation, suggests that the oxide scales of DS2507 possessed a good mechanical integrity and an excellent adhesion to the metallic substrate. Finally, Figure 9d–f shows the scratch tracks of DS2205 at exposure times of 120 h, 300 h and 1600 h, respectively. Conformal cracks and marks were visible when there was through-thickness cracking at the front and sides of the indenter [59]. This was due to the partial ring cracks, which occurred ahead of the indenter and then passed over and pushed into scratch track. These failure mechanisms

in the scratch tracks show that the oxide scales of DS2205 presented a lower adhesion and mechanical integrity compared to those of DS2507.

3.5. Surface Topography of Oxide Scales

The surface topography of oxide scales may be a critical parameter for a possible implementation of these duplex steels in CSP plants. In this sense, the molten salts flow through different components of CSP such as tubes, pipes and tanks, generating a certain friction force between the metal surface and the molten salt. A surface with a poor flatness and high roughness can increase the friction between the oxide scale and molten salt; and therefore, it could contribute to the detachment of oxide scales in operation. This aspect is especially critical when the oxide-substrate adhesion force is not high enough, because the roughness surface could contribute to detach the oxide scale, and consequently, accelerate the corrosion process. Figures 10 and 11 show the surface topographic profiles and the surface roughness parameter (R_a) of the oxide scales, obtained from contact profilometer, formed after exposing duplex and superduplex samples to molten salts for different times. As expected, the polished surfaces of the as-prepared samples, used as references, exhibited typical surface roughness of grinding process (<0.1 μm) with a remarkably flat topographical profile. In contrast, after a few tens and hundreds of hours (24, 120 and 300 h) of exposure to the molten salts, the surfaces of the DS2205 oxide scales exhibited larger roughness with significant irregularities in height and presence of strong hills and valleys (Figures 10a and 11). This could be attributed to the fact that the oxide layer in this first stage of corrosion was formed with a preferential chemical attack in those regions with defects or high surface energy. This strongly irregular topography was significantly increased with the exposure time. The sample exposed for 1600 h presented the surface with the most roughness. On the other side, the oxide scales of DS2507 exhibited lower roughness and flatter oxide layers than DS2205, showing a similar topographic profile with the exposure time as well as roughness values with a low variation after 120 h (Figures 10b and 11).
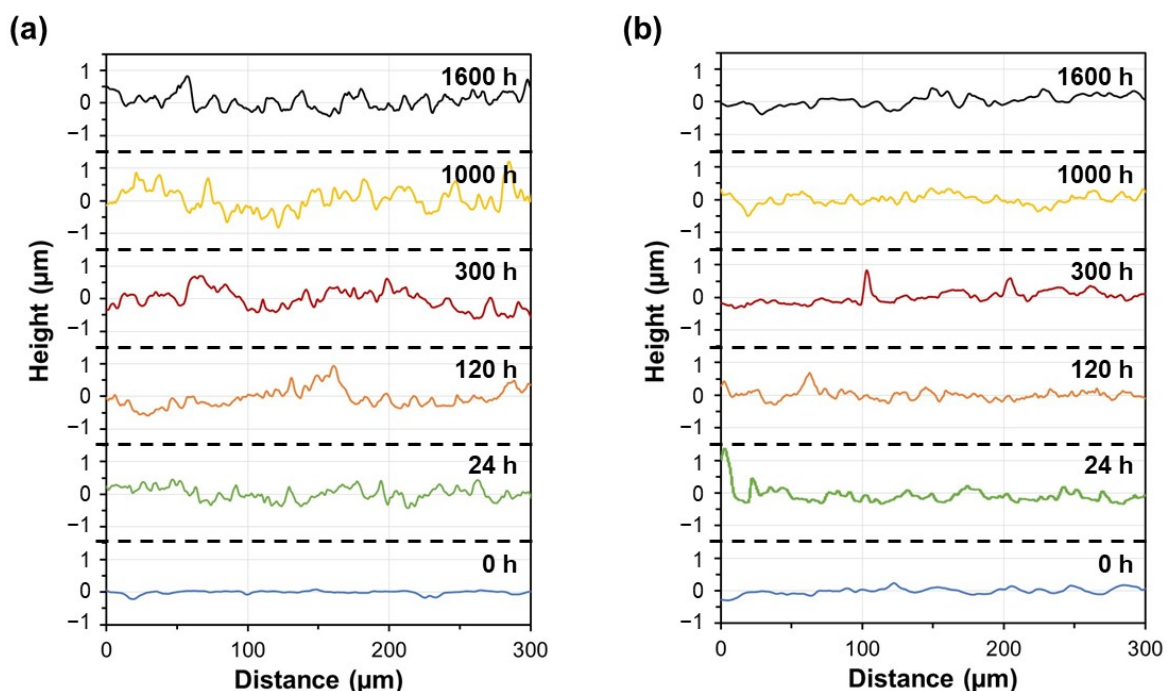

Figure 10. Surface topographic profiles of the oxide scales, obtained from contact profilometer, formed on the: (**a**) DS2205 and (**b**) DS2507, after exposing to molten salts for different times.
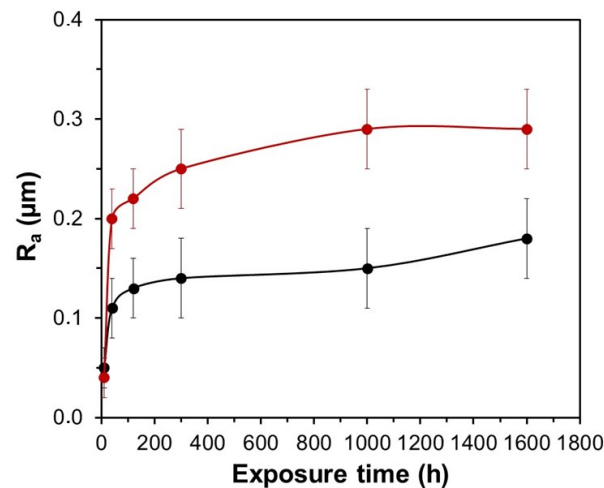
Figure 11. Surface roughness parameter (R_a) of the oxide scales, determined from contact profilometer, formed on the: (red) DS2205 and (black) DS2507, after exposing to molten salts for different times.

4. Conclusions

Duplex stainless steels from grades 2205 and 2507 were evaluated for their compatibility with eutectic Li_2CO_3-K_2CO_3-Na_2CO_3 molten salt at 500 °C in air over the long-term for thermal energy storage applications. The corrosion tests evidenced that DS2507 had a higher corrosion resistance than DS2205, which was attributed to its higher content in Cr, Ni and Mo. Consequently, the relationships between oxide thickness and exposure time for DS2205 and DS2507 samples approximately followed parabolic and cubic growth kinetics, respectively. In both duplex steels, the absence of an intergranular attack on the alloy surface, the non-depletion of the alloying elements from grain boundaries and the homogeneous morphologies of the oxide scales showed that the corrosion proceeded as a uniform degradation, without localized corrosion, on the alloy surface. In this sense, the oxide scales of DS2507 presented a better mechanical integrity and adhesion to the substrate, because scratch tests at the oxide layer/substrate interface did not show important damage, such as cracks, marks and spallation. Therefore, this gives an idea about the high quality of their oxide scales formed at long-term. In contrast, the formation of conformal cracks and marks at the oxide–substrate interface in the scratch track of DS2205 evidenced a lower adhesion to the substrate. The formation of porosity at the oxide scales may be attributed to the significant formation of $LiFeO_2$, and especially $LiFe_5O_8$. The higher content in Cr, Ni and Mo of the oxide scales concentrated near the oxide layer/substrate interface of DSS2705 probably contributed to the formation of an inner oxide layer composed of Cr, Fe, Ni and Mo oxides with remarkable mechanical integrity and adhesion to substrate. Thus, it could also play an important role as a barrier against further oxidation. On the other side, the oxide scales of DS2507 exhibited a lower surface roughness and a flatter oxide layer than those of DS2205. As a result, duplex stainless steel 2205, and especially superduplex 2507, could be promising alternatives for thermal energy storage of those structural components in CSP plants that usually operate with eutectic Li_2CO_3-K_2CO_3-Na_2CO_3 molten salt at 500 °C in air. Future work will be focused on the corrosion evaluation at temperatures above 500 °C, and new strategies for the development of protective oxide films to mitigate the corrosion of duplex stainless steels in contact with molten carbonate salts.

Author Contributions: Conceptualization, M.M. and Ó.F.-A.; methodology, M.M., S.G. and Ó.F.-A.; software, M.M., S.G. and Ó.F.-A.; validation, M.M. and Ó.F.-A.; formal analysis, M.M. and Ó.F.-A.; investigation, M.M., Ó.F.-A. and G.F.; resources, M.M., S.G., F.G.-M., A.M. and G.F.; data curation, M.M., Ó.F.-A. and G.F.; writing—original draft preparation, M.M.; writing—review and editing, M.M., S.G., Ó.F.-A., F.G.-M., A.M. and G.F.; visualization, M.M. and Ó.F.-A.; supervision, M.M. and G.F.; project administration, M.M.; funding acquisition, A.M. and L.L. All authors have read and agreed to the published version of the manuscript.

Data Availability Statement: Not applicable.

Conflicts of Interest: The authors declare no conflict of interest.

References

1. Liu, M.; Steven Tay, N.H.; Bell, S.; Belusko, M.; Jacob, R.; Will, G.; Saman, W.; Bruno, F. Review on Concentrating Solar Power Plants and New Developments in High Temperature Thermal Energy Storage Technologies. *Renew. Sustain. Energy Rev.* **2016**, *53*, 1411–1432. [CrossRef]
2. Lovegrove, K.; Csiro, W.S. Introduction to Concentrating Solar Power (CSP) Technology. *Conc. Sol. Power Technol.* **2012**, 3–15. [CrossRef]
3. Lovegrove, K.; Pye, J. Fundamental Principles of Concentrating Solar Power (CSP) Systems. *Conc. Sol. Power Technol.* **2012**, 16–67. [CrossRef]
4. Liu, M.; Saman, W.; Bruno, F. Review on Storage Materials and Thermal Performance Enhancement Techniques for High Temperature Phase Change Thermal Storage Systems. *Renew. Sustain. Energy Rev.* **2012**, *16*, 2118–2132. [CrossRef]
5. Cabeza, L.F.; Gutierrez, A.; Barreneche, C.; Ushak, S.; Fernández, Á.G.; Inés Fernádez, A.; Grágeda, M. Lithium in Thermal Energy Storage: A State-of-the-Art Review. *Renew. Sustain. Energy Rev.* **2015**, *42*, 1106–1112. [CrossRef]
6. Bauer, T.; Pfleger, N.; Laing, D.; Steinmann, W.D.; Eck, M.; Kaesche, S. High-Temperature Molten Salts for Solar Power Application. In *Molten Salts Chemistry*; Elsevier: Amsterdam, The Netherlands, 2013; pp. 415–438. [CrossRef]
7. Bauer, T.; Odenthal, C.; Bonk, A. Review. Molten Salt Storage for Power Generation. *Chem. Ing. Tech.* **2021**, *93*, 534–546. [CrossRef]
8. Parrado, C.; Marzo, A.; Fuentealba, E.; Fernández, A.G. 2050 LCOE Improvement Using New Molten Salts for Thermal Energy Storage in CSP Plants. *Renew. Sustain. Energy Rev.* **2016**, *57*, 505–514. [CrossRef]
9. Ding, W.; Bauer, T. Progress in Research and Development of Molten Chloride Salt Technology for Next Generation Concentrated Solar Power Plants. *Engineering* **2021**, *7*, 334–347. [CrossRef]
10. Ajdad, H.; Filali Baba, Y.; Al Mers, A.; Merroun, O.; Bouatem, A.; Boutammachte, N.; El Alj, S.; Benyakhlef, S. Thermal and Optical Efficiency Analysis of the Linear Fresnel Concentrator Compound Parabolic Collector Receiver. *J. Sol. Energy Eng. Trans. ASME* **2018**, *140*, 051007. [CrossRef]
11. ur Rehman, T.; Ali, H.M. Experimental Study on the Thermal Behavior of RT-35HC Paraffin within Copper and Iron-Nickel Open Cell Foams: Energy Storage for Thermal Management of Electronics. *Int. J. Heat Mass Transf.* **2020**, *146*, 118852. [CrossRef]
12. Bouadila, S.; Baddadi, S.; ur Rehman, T.; Ayed, R. Experimental Investigation on the Thermal Appraisal of Heat Pipe-Evacuated Tube Collector-Based Water Heating System Integrated with PCM. *Renew. Energy* **2022**, *199*, 382–394. [CrossRef]
13. Filali Baba, Y.; Al Mers, A.; -ur-Rehman, T.; Ajdad, H.; Bouatem, A.; Faik, A.; Bououlid Idrissi, B. No-Vacuum Mono-Tube Compound Parabolic Collector Receiver for Linear Fresnel Concentrator: Numerical and Experimental Approach for Dynamic Behavior Assessment. *Energy Convers. Manag.* **2022**, *268*, 115986. [CrossRef]
14. Sarvghad, M.; Delkasar Maher, S.; Collard, D.; Tassan, M.; Will, G.; Steinberg, T.A. Materials Compatibility for the next Generation of Concentrated Solar Power Plants. *Energy Storage Mater.* **2018**, *14*, 179–198. [CrossRef]
15. Gomez, J.C. *High-Temperature Phase Change Materials (PCM) Candidates for Thermal Energy Storage (TES) Applications*; National Renewable Energy Lab. (NREL): Golden, CO, USA, 2011. [CrossRef]
16. Kenisarin, M.M. High-Temperature Phase Change Materials for Thermal Energy Storage. *Renew. Sustain. Energy Rev.* **2010**, *14*, 955–970. [CrossRef]
17. Myers, P.D.; Goswami, D.Y. Thermal Energy Storage Using Chloride Salts and Their Eutectics. *Appl. Therm. Eng.* **2016**, *109*, 889–900. [CrossRef]
18. Mehos, M.; Turchi, C.; Vidal, J.; Wagner, M.; Ma, Z.; Ho, C.; Kolb, W.; Andraka, C.; Kruizenga, A. *Concentrating Solar Power Gen3 Demonstration Roadmap*; NREL/TP-5500-67464; National Renewable Energy Lab. (NREL): Golden, CO, USA, 2017; pp. 1–140. [CrossRef]
19. Turchi, C.S.; Vidal, J.; Bauer, M. Molten Salt Power Towers Operating at 600–650 °C: Salt Selection and Cost Benefits. *Sol. Energy* **2018**, *164*, 38–46. [CrossRef]
20. Nunes, V.M.B.; Lourenço, M.J.V.; Santos, F.J.V.; Nieto de Castro, C.A. Molten Alkali Carbonates as Alternative Engineering Fluids for High Temperature Applications. *Appl. Energy* **2019**, *242*, 1626–1633. [CrossRef]
21. Mineral Requirements for Clean Energy Transitions—The Role of Critical Minerals in Clean Energy Transitions—Analysis—IEA. Available online: https://www.iea.org/reports/the-role-of-critical-minerals-in-clean-energy-transitions/mineral-requirements-for-clean-energy-transitions (accessed on 31 August 2022).
22. Greim, P.; Solomon, A.A.; Breyer, C. Assessment of Lithium Criticality in the Global Energy Transition and Addressing Policy Gaps in Transportation. *Nat. Commun.* **2020**, *11*, 1–11. [CrossRef]
23. U.S. Department of Energy. Federal Consortium for Advanced Batteries. National Blueprint for Lithium Batteries Executive Summary 2021–2030. 2021; pp. 1–24. Available online: www.energy.gov/eere/vehicles (accessed on 14 December 2022).

24.   Beyond Lithium: Other Potential Technologies That Battery Manufacturers Are Betting on | CIC EnergiGUNE. Available online: https://cicenergigune.com/en/blog/beyond-lithium-technologies-battery-manufacturers (accessed on 31 August 2022).

25.   Chi, X.; Zhang, Y.; Hao, F.; Kmiec, S.; Dong, H.; Xu, R.; Zhao, K.; Ai, Q.; Terlier, T.; Wang, L.; et al. An Electrochemically Stable Homogeneous Glassy Electrolyte Formed at Room Temperature for All-Solid-State Sodium Batteries. *Nat. Commun.* **2022**, *13*, 1–11. [CrossRef]

26.   Fereres, S.; Prieto, C.; Giménez-Gavarrell, P.; Rodríguez, A.; Sánchez-Jiménez, P.E.; Pérez-Maqueda, L.A. Molten Carbonate Salts for Advanced Solar Thermal Energy Power Plants: Cover Gas Effect on Fluid Thermal Stability. *Sol. Energy Mater. Sol. Cells* **2018**, *188*, 119–126. [CrossRef]

27.   Prieto, C.; Fereres, S.; Ruiz-Cabañas, F.J.; Rodriguez-Sanchez, A.; Montero, C. Carbonate Molten Salt Solar Thermal Pilot Facility: Plant Design, Commissioning and Operation up to 700 °C. *Renew. Energy* **2020**, *151*, 528–541. [CrossRef]

28.   Sarvghad, M.; Steinberg, T.A.; Will, G. Corrosion of Steel Alloys in Eutectic NaCl+Na$_2$CO$_3$ at 700 °C and Li$_2$CO$_3$ + K$_2$CO$_3$ + Na$_2$CO$_3$ at 450 °C for Thermal Energy Storage. *Sol. Energy Mater. Sol. Cells* **2017**, *170*, 48–59. [CrossRef]

29.   Sarvghad, M.; Will, G.; Steinberg, T.A. Corrosion of Inconel 601 in Molten Salts for Thermal Energy Storage. *Sol. Energy Mater. Sol. Cells* **2017**, *172*, 220–229. [CrossRef]

30.   de Miguel, M.T.; Encinas-Sánchez, V.; Lasanta, M.I.; García-Martín, G.; Pérez, F.J. Corrosion Resistance of HR3C to a Carbonate Molten Salt for Energy Storage Applications in CSP Plants. *Sol. Energy Mater. Sol. Cells* **2016**, *157*, 966–972. [CrossRef]

31.   Gallardo-González, J.; Martínez, M.; Barreneche, C.; Fernández, A.I.; Liu, M.; Tay, N.H.S.; Bruno, F.; Segarra, M. Corrosion of AISI316 as Containment Material for Latent Heat Thermal Energy Storage Systems Based on Carbonates. *Sol. Energy Mater. Sol. Cells* **2018**, *186*, 1–8. [CrossRef]

32.   Sah, S.P. Corrosion of 304 Stainless Steel in Carbonates Melt– a State of Enhanced Dissolution of Corrosion Products. *Corros. Sci.* **2020**, *169*, 108535. [CrossRef]

33.   Fernández, A.G.; Pineda, F.; Walczak, M.; Cabeza, L.F. Corrosion Evaluation of Alumina-Forming Alloys in Carbonate Molten Salt for CSP Plants. *Renew. Energy* **2019**, *140*, 227–233. [CrossRef]

34.   Grosu, Y.; Anagnostopoulos, A.; Navarro, M.E.; Ding, Y.; Faik, A. Inhibiting Hot Corrosion of Molten Li$_2$CO$_3$-Na$_2$CO$_3$-K$_2$CO$_3$ Salt through Graphitization of Construction Materials for Concentrated Solar Power. *Sol. Energy Mater. Sol. Cells* **2020**, *215*, 110650. [CrossRef]

35.   Rouillard, F.; Charten, F.; Moine, G. Corrosion Behavior of Different Metallic Materials in Supercritical Carbon Dioxide at 550 °C and 250 Bars. *Corrosion* **2011**, *67*, 095001–095007. [CrossRef]

36.   Chan, K.W.; Tjong, S.C. Effect of Secondary Phase Precipitation on the Corrosion Behavior of Duplex Stainless Steels. *Materials* **2014**, *7*, 5268–5304. [CrossRef]

37.   Solomon, H.D. Stainless Steels: Duplex. *Encycl. Mater. Sci. Technol.* **2001**, 8802–8804. [CrossRef]

38.   Paulraj, P.; Garg, R. Effect of Intermetallic Phases on Corrosion Behavior and Mechanical Properties of Duplex Stainless Steel and Super-Duplex Stainless Steel. *Adv. Sci. Technol. Res. J.* **2015**, *9*, 87–105. [CrossRef]

39.   Sarvghad, M.; Will, G.; Steinberg, T.A. Corrosion of Steel Alloys in Molten NaCl + Na$_2$SO$_4$ at 700 °C for Thermal Energy Storage. *Sol. Energy Mater. Sol. Cells* **2018**, *179*, 207–216. [CrossRef]

40.   Llanes, L.; Mateo, A.; Villechaise, P.; Méndez, J.; Anglada, M. Effect of Testing Atmosphere (Air/in Vacuo) on Low Cycle Fatigue Characteristics of a Duplex Stainless Steel. *Int. J. Fatigue* **1999**, *21*, S119–S125. [CrossRef]

41.   Gironès, A.; Villechaise, P.; Mateo, A.; Anglada, M.; Méndez, J. EBSD Studies on the Influence of Texture on the Surface Damage Mechanisms Developed in Cyclically Loaded Aged Duplex Stainless Steels. *Mater. Sci. Eng. A* **2004**, *387–389*, 516–521. [CrossRef]

42.   Fargas, G.; Akdut, N.; Anglada, M.; Mateo, A. Microstructural Evolution during Industrial Rolling of a Duplex Stainless Steel. *ISIJ Int.* **2008**, *48*, 1596–1602. [CrossRef]

43.   Fargas, G.; Anglada, M.; Mateo, A. Effect of the Annealing Temperature on the Mechanical Properties, Formability and Corrosion Resistance of Hot-Rolled Duplex Stainless Steel. *J. Mater. Process. Technol.* **2009**, *209*, 1770–1782. [CrossRef]

44.   Verma, J.; Taiwade, R.V. Effect of Welding Processes and Conditions on the Microstructure, Mechanical Properties and Corrosion Resistance of Duplex Stainless Steel Weldments—A Review. *J. Manuf. Process.* **2017**, *25*, 134–152. [CrossRef]

45.   Besharatloo, H.; Carpio, M.; Cabrera, J.M.; Mateo, A.M.; Fargas, G.; Wheeler, J.M.; Roa, J.J.; Llanes, L. Novel Mechanical Characterization of Austenite and Ferrite Phases within Duplex Stainless Steel. *Metals* **2020**, *10*, 1352. [CrossRef]

46.   Maslak, M.; Stankiewicz, M.; Slazak, B. Duplex Steels Used in Building Structures and Their Resistance to Chloride Corrosion. *Materials* **2021**, *14*, 5666. [CrossRef]

47.   Morales, M.; Chimenos, J.M.; Fernández, A.I.; Segarra, M. Materials Selection for Superheater Tubes in Municipal Solid Waste Incineration Plants. *J. Mater. Eng. Perform.* **2014**, *23*, 3207–3214. [CrossRef]

48.   Mateo, A.; Heredero, F.; Fargas, G. Failure Investigation of a Centrifuge Duplex Stainless Steel Basket. *Eng. Fail. Anal.* **2011**, *18*, 2165–2178. [CrossRef]

49.   Hara, T.; Semba, H.; Amaya, H. Pipe and Tube Steels for Oil and Gas Industry and Thermal Power Plant. *Encycl. Mater. Met. Alloy.* **2022**, 140–152. [CrossRef]

50.   Wu, Y.T.; Ren, N.; Wang, T.; Ma, C. fang Experimental Study on Optimized Composition of Mixed Carbonate Salt for Sensible Heat Storage in Solar Thermal Power Plant. *Sol. Energy* **2011**, *85*, 1957–1966. [CrossRef]

51.   Chen, C.; Tran, T.; Olivares, R.; Wright, S.; Sun, S. Coupled Experimental Study and Thermodynamic Modeling of Melting Point and Thermal Stability of Li$_2$CO$_3$-Na$_2$CO$_3$-K$_2$CO$_3$ Based Salts. *J. Sol. Energy Eng. Trans. ASME* **2014**, *136*. [CrossRef]

52. Itoh, M. Time-Dependent Power Laws in the Oxidation and Corrosion of Metals and Alloys. *Sci. Rep.* **2022**, *12*, 1–9. [CrossRef]

53. Morcillo, M.; Chico, B.; Díaz, I.; Cano, H.; De La Fuente, D. Atmospheric corrosion data of weathering steels. A review. *Corros. Sci.* **2013**, *77*, 6–24. [CrossRef]

54. Biedenkopf, P.; Spiegel, M.; Grabke, H.J. The Corrosion Behavior of Fe-Cr Alloys Containing Co, Mn, and/or Ni and of a Co-Base Alloy in the Presence of Molten (Li,K)-Carbonate. *Mater. Corros.* **1997**, *48*, 731–743. [CrossRef]

55. Corrosion Phenomena of Alloys and Electrode Materials in Molten Carbonate Fuel Cells—Biedenkopf—2000—Materials and Corrosion—Wiley Online Library. Available online: https://onlinelibrary-wiley-com.recursos.biblioteca.upc.edu/doi/abs/10.1002/%28SICI%291521-4176%28200005%2951%3A5%3C287%3A%3AAID-MACO287%3E3.0.CO%3B2-8 (accessed on 3 December 2022).

56. Tan, L.; Yang, Y.; Allen, T.R. Oxidation Behavior of Iron-Based Alloy HCM12A Exposed in Supercritical Water. *Corros. Sci.* **2006**, *48*, 3123–3138. [CrossRef]

57. Soleimani Dorcheh, A.; Durham, R.N.; Galetz, M.C. Corrosion Behavior of Stainless and Low-Chromium Steels and IN625 in Molten Nitrate Salts at 600 °C. *Sol. Energy Mater. Sol. Cells* **2016**, *144*, 109–116. [CrossRef]

58. Morales, M.; Chimenos, J.M.; Espiell, F.; Segarra, M. The Effect of Temperature on Mechanical Properties of Oxide Scales Formed on a Carbon Steel in a Simulated Municipal Solid Waste Incineration Environment. *Surf. Coatings Technol.* **2014**, *238*, 51–57. [CrossRef]

59. Farhan, M.S. A Review on Adhesion Strength of Single and Multilayer Coatings and the Evaluation Method. *Wasit J. Eng. Sci.* **2016**, *4*, 1–27.